Advanced Antibacterial Materials
https://www.sciltp.com/journals/aam

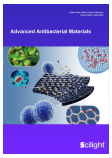

Article

Bacteria-Powered Photodynamic Amplification on Nano-Bio Interface for Selective Pathogen Killing and Tissue Regeneration

Jieni Fu [1,2,3], Chaofeng Wang [1], Congyang Mao [2], Hui Jiang [3], Jie Shen [4], Zhaoyang Li [3], Yanqin Liang [3], Shengli Zhu [3], Zhenduo Cui [3] and Xiangmei Liu [1,2,*]

[1] School of Health Science & Biomedical Engineering, Hebei University of Technology, Xiping Avenue 5340#, Tianjin 300401, China
[2] Biomedical Materials Engineering Research Center, Hubei Key Laboratory of Polymer Materials, Ministry-of-Education Key Laboratory for the Green Preparation and Application of Functional Materials, School of Materials Science & Engineering, State Key Laboratory of Biocatalysis and Enzyme Engineering, Hubei University, Youyi Avenue 368#, Wuhan 430062, China
[3] School of Materials Science & Engineering, the Key Laboratory of Advanced Ceramics and Machining Technology by the Ministry of Education of China, Tianjin University, Yaguan Road 135#, Tianjin 300072, China
[4] Shenzhen Key Laboratory of Spine Surgery, Department of Spine Surgery, Peking University Shenzhen Hospital, Lianhua Road 1120#, Shenzhen 518036, China
* Correspondence: liuxiangmei1978@163.com

How To Cite: Fu, J.; Wang, C.; Mao, C.; et al. Bacteria-Powered Photodynamic Amplification on Nano-Bio Interface for Selective Pathogen Killing and Tissue Regeneration. *Advanced Antibacterial Materials* **2025**.

Received: 29 June 2025
Revised: 4 July 2025
Accepted: 14 July 2025
Published: 22 July 2025

Abstract: Photodynamic therapy can be used to clear bacterial infections. However, light disinfection primarily relies on reactive oxygen species (ROS), which are nonselective, leading to undesired damage to normal cells. Therefore, developing a photosensitizer that can selectively kill bacteria and protect normal cells is highly desirable based on the structural difference between normal cells and bacteria. In this study, a bacterial redox potential-boosted photocatalytic concept is proposed. Here, we designed a selectively bacteria-killing photosensitizer, hydroxyapatite/MoS_2 coating in Ti6 implant (HA/MoS_2-Ti6), which could accept the electrons from bacteria due to the potential difference between HA/MoS_2 and the bacterial outer membrane. Then it further boosted the separation of electrons and holes of HA/MoS_2 produced by 660 nm light irradiation, which enhanced the photocatalytic activity of HA/MoS_2-Ti6. Density functional theory calculation further demonstrated the complete electron transfer circulation between HA/MoS_2-Ti6 and the bacterial outer membrane. The produced ROS and changed electrons transfer pathway altered bacterial membrane potential and intracellular ROS, leading to bacterial death (92.99 ± 0.84% against *Staphylococcus aureus* and 94.70 ± 3.60% against *Escherichia coli*). Meanwhile, HA/MoS_2-Ti6 has great biocompatibility with Raw 264.7, L929, and MC3T3-E1 with/without light irradiation. HA/MoS_2-Ti6 can also enhance MC3T3-E1 into osteoblasts due to the osteoinduction of HA. HA/MoS_2-Ti6 induced macrophages to differentiate into M2 under light irradiation. The strategy-based nano-bio interface offered a new platform to clear microbes and enhance cell differentiation simultaneously.

Keywords: phototherapy; selective bacterial killing; bacterial redox potential; HA/MoS_2

1. Introduction

The antibiotics are commonly used to inhibit or kill bacteria in clinical [1,2]. However, overuse of antibiotics can stimulate the development of antibiotic resistance and inhibit host immune responses [3–5]. Photodynamic therapy (PDT) is an attractive strategy to solve bacterial antimicrobial resistance. The related mechanism involves the photosensitizer absorbing light to produce reactive oxygen species (ROS). The ROS subsequently causes microbe inactivation by damaging essential macromolecules [6]. However, ROS can also damage the normal cells surrounding the implant. It is desirable to acquire selected PDT methods against bacteria and protect normal cells simultaneously.

Current strategies are to use bacteria-targeted photosensitizers [7]. This strategy often conjugates photosensitizers with bacteria-specific antibodies [8]. However, the targeted efficiency of bacteria-targeted photosensitizers is limited, which may hinder their clinical application [7]. Luckily, microorganisms own a transmembrane redox potential due to electron transfer in bacterial respiration [9–11]. The bacteria possessed the biological redox potential (BRP) due to the disulfide bonds on the bacterial membrane, whose range was −4.12 eV to −4.84 eV [12,13]. However, the BRP for cells is mitochondria-associated redox potentials, and the potential is at mitochondria, not at the cell membrane [14]. Designing biological redox potential (BRP)-matched photocatalysts might be an attractive method to selectively kill pathogens without harming normal cells.

The primary light-harvesting materials matched with BRP are generally inorganic semiconductors, such as cadmium sulfide (CdS) [15,16], cobalt phosphate (CoP) [17], indium phosphide (InP) [18], and gold nanoclusters (AuNCs) [19]. However, inorganic semiconductors mainly include heavy metals, which have toxic effects on tissue in vivo. Thus, it is attractive to seek semiconductors with outstanding biocompatibility to absorb light and transfer electrons from microorganisms to boost PDT.

Molybdenum sulfide (MoS_2), a typical layered transition-metal dichalcogenide, shows excellent activity in catalysts and sensors [20]. MoS_2 nanosheets can effectively harvest visible light. The bandgap of MoS_2 nanosheets is 1.3 eV for the indirect bandgap and 1.9 eV for the direct bandgap [6], which is unsuitable as an electron acceptor [20,21]. Therefore, it is a promising approach to introduce biocompatible material to modify the bandgap to match with BRP. HA is nontoxic as an osteoconductive material. Meanwhile, HA can improve the photocatalytic effect of semiconductors by accommodating electrons to enhance the separation of electrons and holes [22]. The bandgap of HA ranges from 4.5 eV to 5.4 eV [22]. We previously used HA/MoS_2 heterojunction whose potential could match the BRP to make the electron transfer occur between bacteria and HA/MoS_2 heterojunction [23]. However, whether the electron transfer process could amplify PDT is still unknown.

In this work, we presented a general and biocompatible platform to use the bacterial electron flux to directly boost ROS production of HA/MoS_2-Ti6 under 660 nm light irradiation without inhibiting the growth of Raw 264.7, L929, and MC3T3-E1. Compared with MoS_2, the photocatalytic activity of HA/MoS_2 heterojunction was enhanced due to the electrons from MoS_2 to HA, based on density functional theory (DFT) calculation. Next, when bacteria contacted HA/MoS_2-Ti6, the electrons from bacteria during the aerobic respiration were transferred to HA/MoS_2-Ti6. The process was analyzed via DFT calculation, and we named the material as bacteria-HA/MoS_2-Ti6 heterojunction. Living bacteria then boosted the photocatalytic activity of HA/MoS_2-Ti6 under 660 nm light irradiation, which was demonstrated via experimental data. The antibacterial activity against Staphylococcus aureus (*S. aureus*) and Escherichia coli (*E. coli*) was 92.99 ± 0.84% and 94.7 ± 3.6% under 660 nm light irradiation for 15 min. Meanwhile, HA/MoS_2-Ti6 showed great biocompatibility towards Raw 264.7, L929, and MC3T3-E1. HA/MoS_2-Ti6 could also enhance MC3T3-E1 into osteoblasts due to the osteoinduction of HA. And when Raw 264.7 cells were cocultured with HA/MoS_2-Ti6 under light irradiation, the Raw 264.7 tended to differentiate into M2 due to the redox potential of HA/MoS_2-Ti6. Our approach offered a strategy for clear infection by taking advantage of bacterial metabolism (Scheme 1). The bacterial respiration-boosted photocatalysis, clearing infection deeply, inspired the design of antibacterial materials and paved the way for understanding the antibacterial mechanism.

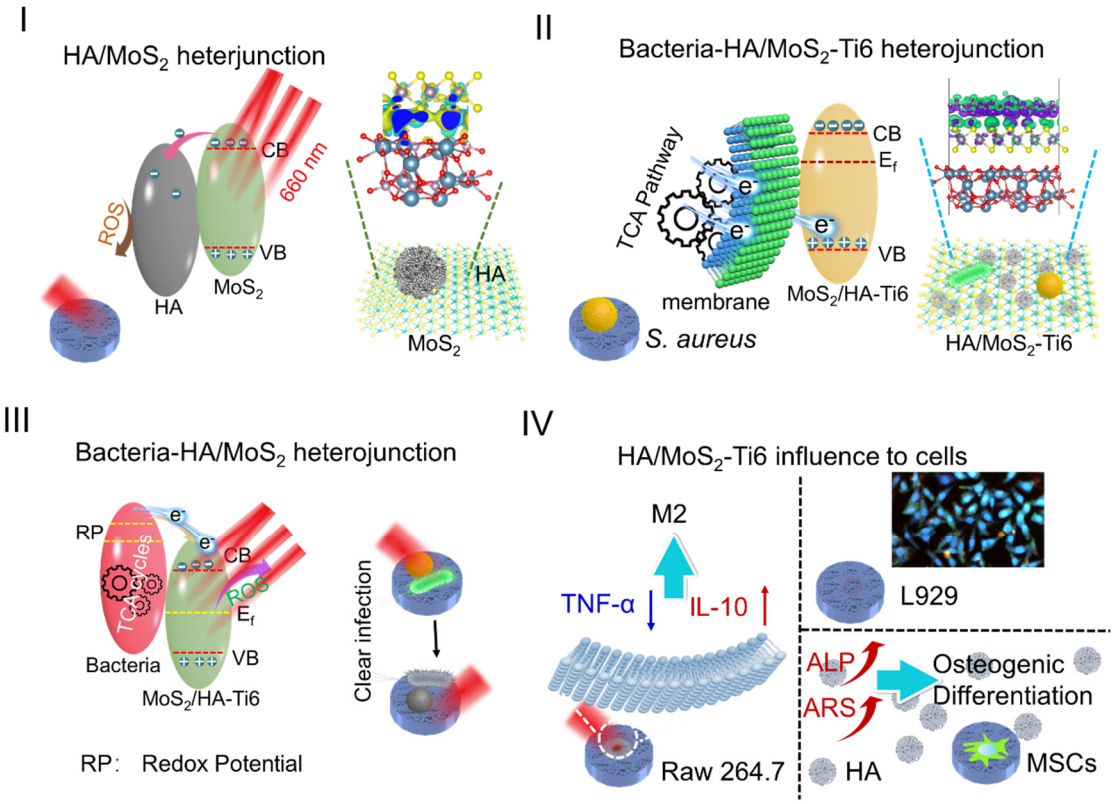

Scheme 1. Schematic representation of bacteria-HA/MoS_2 heterojunction for selective pathogen killing and tissue regeneration.

2. Materials and Methods

2.1. Materials

Ti6Al4V (Ti6) plates (2.5 mm × Φ6 mm and 2.5 mm × Φ20 mm) were obtained from Baosteel Co. Ltd. (Shanghai, China). Hydroxyapatite (HA) (purity > 99.5%) and MoS_2 were purchased from Aladdin Reagent (Shanghai, China). 2,7-Dichlorodihydrofluorescein diacetate (DCFH) and phosphate buffer solution (PBS) were from Beyotime Biotechnology (Shanghai, China). MTT, Triton X-100, and BCA protein assay kit were from Solarbio (Beijing, China). The alkaline phosphatase assay kit was from the NJJCBIO company (Nanjing, China). Dimethyl sulfoxide (DMSO) and NaCl were from Sinopharm Chemical Reagent. Co., Ltd. (Shanghai, China).

2.2. Preparation of HA-Ti6, MoS_2-Ti6, and HA/MoS_2-Ti6

Ti6 plates were first polished through silicon carbide (SiC) sandpapers of 240, 400, 600, and 800 grits, then ultrasonically cleaned with ethanol and deionized (DI) water for 15 min, respectively. Then, HA (100 mg) and MoS_2 (100 mg) were dispersed in 10 mL deionized (DI) water via vigorous ultrasonication for 60 min. Next, 60 μL of different solutions (HA solution and MoS_2 solution) were dipped onto the surface of the Ti6 plate, respectively. Then, they are dried in an oven at 50 ℃ for 4 h to form a pre-coating of HA-Ti6 and pre-coating MoS_2-Ti6. Pre-coated HA-Ti6 samples and pre-coated MoS_2-Ti6 samples were placed on a CW 2 kW Nd: YAG laser (wavelength 1.06 μm, LUMONICS, JHM-1GY-300B), respectively, and then the samples were exposed to the laser instrument. And the optimal parameters were laser current = 95 A, pulse width = 2 ms, frequency = 20 Hz, spot diameter = 0.6 mm, and scanning speed = 5 mm/s. After selective laser melting treatment, the samples were named HA-Ti6 and untreated MoS_2–Ti6. Similarly, HA (5 g/mL) and MoS_2 (5 g/mL) were evenly dispersed with DI water. Next, the solution was dropped onto the Ti6 plate surface and dried in an oven, which was nominated pre-coating HA/MoS_2-Ti6. And then, the samples were subjected to a selective laser melting process to form a coating on the surface of Ti6. Next, untreated MoS_2-Ti6 and HA/MoS_2-Ti6 samples prepared after laser cladding were sulfurated using the CVD method. Specifically, sulfur powder (0.3 g) was put in a quartz tube filled with a nitrogen atmosphere to sulfurate samples, and the atmospheric pressure was maintained. The parameters of the vacuum tube furnace were set. The heating rate was 10 ℃/min to reach 750 ℃ for 70 min via CVD sulfuration treatment.

2.3. Characterization of Ti6, HA-Ti6, MoS_2-Ti6, and HA/MoS_2-Ti6

The surface morphologies and cross-sectional images of different samples were obtained from FE-SEM (Zeiss Sigma 500, Carl Zeiss AG, Oberkochen, Germany), SEM (JSM-6510LV, JEOL, Tokyo, Japan), and TEM (Tecnai G20, FEI, Lexington, KY, USA). XRD examined the crystal structure of the samples with Bruker diffractometer (D8 Advance, Germany) using Cu Kα radiation (λ = 0.15406 nm). Water contact angles (JC2000D Contact Angle system, shzhongchen, Shanghai, China) analysis was conducted to analyze the hydrophilic property of surfaces. The surface elemental composition of the samples was obtained using XPS (ESCALAB 250Xi, Thermo Scientific, Waltham, MA, USA). PL (LS-55, American PE) with the excitation wavelength of 325 nm was used to obtain the samples' photocatalytic effect. Redox (E_h) measurements were performed with a Milwaukee MW500 ORP meter, fitted with a Milwaukee SE300 ORP probe, and E_h values were collected using an Ag/AgCl in saturated KCl reference electrode.

2.4. DFT Calculations Method

Vienna Ab initio Simulation Package(VASP) with the projector augmented wave (PAW) method was used to perform the samples' first-principles DFT calculations [24,25]. The generalized gradient approximation (GGA) of Perdew-Burke-Ernzerhof (PBE) functional was taken advantage of to treat exchange-functional [26]. The energy cutoff for the plane-wave basis expansion was set to 450 eV, and the force on each atom less than 0.03 eV/Å was selected for the convergence criterion of geometry relaxation. A single Γ point sampled the Brillouin-zone integration. The self-consistent calculations apply a convergence energy threshold of 10^{-4} eV. The DFT-D3 method was employed to consider the van der Waals interaction [27].

2.5. ROS Measurement in the Cell-Free System

The DCFH was used to detect the ROS production content. In brief, the DCFH working solution was obtained through shocking for 30 min after adding 50 μL DCFH-DA, mixing with 450 μL absolute ethanol in 1.5 mL 0.01 M NaOH in the dark. Then, the working solution was added to the surface of different samples. Next, the samples were irradiated by 660 nm visible light with a laser power of 260 mW (MRL-III-660Dnm-500mW-16090712, China). Finally, the data were obtained from a microplate reader (SpectraMax i3, Molecular Devices, San Jose, CA, USA) at an excitation wavelength of 488 nm and an emission wavelength of 525 nm.

DPBF was used to detect $^1O_2$, and the data were obtained from a microplate reader (SpectraMax i3, Molecular Devices) at 410 nm. NBT (2.5×10^{-5} M dissolved in DMSO solution) was used to detect O_2^-, and the data were obtained from a microplate reader (SpectraMax i3, Molecular Devices) at 405 nm. 0.5mM TA (dissolved in 2 mM NaOH solution) was used to measure ·OH at an excitation wavelength of 425 nm and emission wavelength of 315 nm.

2.6. In Vitro Antibacterial Assay

Bacterial spread plate. The spread plate method was used to study the antibacterial activity of the samples (including Ti6, HA-Ti6, MoS_2-Ti6, HA/MoS_2-Ti6) under 660 nm light irradiation. *E. coli* (Gram-negative, ATCC25922) and *S. aureus* (Gram-positive, ATCC29213) were used for antibacterial experiments. All bacteria were cultured in an aseptic Luria-Bertani (LB) medium. The details were as follows: all the samples were put into 96-well plates separately. And 200 μL of bacterial suspension (*E. coli* and *S. aureus*) with 1×10^5 colony-forming units (CFU)/mL was added into each well. Then, the samples were divided into two groups; one group was irradiated for 15 min by 660 nm visible light with a laser power of 260 mW, and the other was cultured for 15 min in the dark. After irradiation, the bacterial suspension in each hole was diluted 100-fold by sterile PBS, and 20 μL of the diluted bacterial suspension was drawn from each hole to spread on LB agar plates and incubated in the oven at 37 °C for 24 h.

Bacterial morphology. The bacteria on the samples were fixed with 2.5% glutaraldehyde for 2 h after different treatments. Then, it was washed thrice with PBS and dehydrated with varying ethanol concentrations (30, 50, 70, 90, and 100 *v*/*v* %) for 15 min each. Finally, the bacterial morphologies on the samples were observed by SEM.

Live/dead staining test for bacteria. Bacterial solution (10^7 CFU·mL^{-1}) was added to the surface of different samples (Ti6, HA-Ti6, MoS_2-Ti6, and HA/MoS_2-Ti6) in 96 wells. Then, the bacteria were treated with SYTO9 and PI (LIVE/DEAD Baclight Bacterial Viability Kit, Beyotime, for microscopy & quantitative assays) for 15 min after performing different treatments (with or without irradiation). Finally, the pictures were obtained through an inverted fluorescence microscope (IFM, Olympus, IX73).

Membrane potential assay. As for *S. aureus* and *E. coli*, bacterial solution (10^7 CFU·mL^{-1}) was added on the surface of different samples (Ti6, HA-Ti6, MoS_2-Ti6, and HA/MoS_2-Ti6) in 96 wells. After performing the

different treatments, the DiBAC4(3) (5 μM) was added to the LB medium and cultured for 30 min at 37 °C. Finally, the pictures were obtained through an inverted fluorescence microscope (IFM, Olympus, IX73).

ROS detection in bacteria. Bacterial solution (10^7 CFU·mL^{-1}) was added to the surface of different samples (Ti6, HA-Ti6, MoS_2-Ti6, and HA/MoS_2-Ti6) in 96 wells. After performing the different treatments, the DCFH-DA (10 μM) was added to PBS and cultured for 30 min at 37 °C. Finally, the pictures were obtained through an inverted fluorescence microscope (IFM, Olympus, IX73).

2.7. In Vitro Biological Performance Evaluation

MTT assay. The sterilized samples were put into 96-well plates, and 200 μL MC3T3-E1(1×10^5 cells/mL), L929 (1×10^5 cells/mL), or Raw 264.7 (1×10^4 cells/mL) were added into the plates. Then, each type of sample was divided into two groups; one group was irradiated by 660 nm visible light with a laser power of 260 mW, and the other was without 660 nm visible light. The cells were cultured on samples for 1, 3, and 7 days under the same conditions. After that, the culture medium was added and the 100 μL 0.5 mg/mL MTT (dissolved MTT powder in pH 7.4 PBS solution) solution into each well and incubated for 4 h at 37 °C in an atmosphere of 5% CO_2 and 95% air until a purple precipitate appeared. The MTT solution was removed, and 100 μL of DMSO was added to each well with continuous shaking for 15 min to dissolve the purple precipitate. Finally, the samples were taken out, and the OD of the liquid was tested at 490 nm or 570 nm with a microplate reader. For the MTT tests of samples with light irradiation, after cell culturing for 12 h with samples as mentioned above, samples with cells were irradiated for 15 min with 660 nm visible light, and then continued to culture under the same conditions with normal MTT tests. The medium was renewed every two days.

ALP activity. The sterilized samples were put into 96-well plates, and 20,000 cells/well MC3T3-E1 cells were added. And then, the cells were cultured on samples for 3, 7, and 14 days under the same conditions. The growth medium was renewed every two days. The growth medium was removed at the appropriate time point, and 1% Triton X-100 was added. The ALP activity was measured with an alkaline phosphatase (ALP/AKP) assay kit (Nanjing Jiancheng Bioengineering Institute, Nanjing, China), and the manual followed the detailed steps. Besides, the protein content of the cell in each well was tested using the BCA protein assay kit (Solarbio) at 562 nm on a microplate reader, which can determine the ALP activity per unit protein.

Elisa assay. Protein expression of IL-10 and TNF-α was measured by enzyme-linked immunosorbent assay (ELISA) kits (Shanghai Enzyme-linked Biotechnology, Shanghai, China).

Matrix mineralization. The MC3T3-E1 cells were added to the 96-well plate (2000 cells/well) before different samples were placed in the 96-well plate. The growth medium was replaced with osteogenic extract medium (growth medium with 10 mM β-glycerol phosphate, 10^{-8} M dexamethasone, and 50 μg/mL ascorbic acid). The medium was refreshed every two days. After 10 and 21 days of culturing, the samples were rinsed with PBS 3 times and then fixed in 4% paraformaldehyde for 1 h. Afterward, the samples were stained with 2% Alizarin Red solution (pH 4.2) for 10 min and rinsed several times with PBS. The calcium nodule staining was viewed by the SONY α2 camera. 10% hexadecylpyridinium chloride (*w*/*w*) was further used to dissolve the mineralized nodules. And the OD values were measured by a microplate reader at a wavelength of 562 nm.

Cell morphology. The MC3T3-E1 or L929 cells were added to the 96-well plate (2000 cells/well) before different samples were placed in the 96-well plate, and the growth media was removed and fixed cells with 4% formaldehyde solution after culturing for one day. Then, the cell morphologies on the samples were stained with 4′,6-diamidino-2-phenylindole (nucleus, YiSen, Shanghai, China) and FITC-conjugated phalloidin (actin, YiSen, Shanghai, China). Finally, the images were obtained by an inverted fluorescence microscope (IFM; Olympus, IX73, Tokyo, Japan).

2.8. In Vivo Subcutaneous Infection Model and Treatment

The SD rats (10–12 weeks old, about 350 g) used in vivo antibacterial experiment were from Beijing Huafukang Biotechnology Company. All the animal experiments followed the guidelines of the Tianjin Medical Experimental Animal Care, and animal protocols were approved by the Institutional Animal Care and Use Comittee of Yi Shengyuan Gene Technology (Tianjin) Co., Ltd. (protocol number YSY-DWLL-2024712). 12 male SD rats were randomly divided into two groups (n = 6 per group): the Ti-Off and HA/MoS_2-Ti6-On groups (HA/MoS_2-Ti6 + 660 nm light treatment).

First, pentobarbital sodium salt solution (1% *w*/*w*) was used to anesthetize SD rats before surgery. Meanwhile, 20 μL *S. aureus* of 1×10^7 CFU/mL was dropped onto the surface of Ti6 and HA/MoS_2-Ti. Then, the bacteria samples were implanted subcutaneously into the subcutaneous tissue on the back of SD rats. The Ti-Off group was placed Ti6 with *S. aureus* into subcutaneous tissue and did not receive treatment. The HA/MoS_2-Ti6-On group

was placed HA/MoS_2-Ti6 with *S. aureus* into subcutaneous tissue and was irradiated for 15 min by 660 nm visible light with a laser power of 260 mW. After two days, the SD rats were sacrificed, and their blood was collected for blood tests. The tissues around different implants were collected for H&E and Giemsa staining. Moreover, the heart, liver, spleen, lung, and kidneys were collected for H&E staining.

2.10. Statistical Analysis

All the quantitative data in each experiment were evaluated and analyzed by one-way or two-way analysis of variance and expressed as the mean values ± standard deviations from at least three independent experiments. * $p < 0.05$, ** $p < 0.01$, *** $p < 0.001$, and **** $p < 0.0001$ were considered statistically significant.

3. Results and Discussion

3.1. Characterization of HA/MoS_2-Ti6

The Ti6 plate was coated with HA/MoS_2 film after through selective laser melting (SLM) and chemical vapor deposition (CVD) (Figure 1a). The Ti6 plate was dropped into the HA/MoS_2 solution and then dried at 60 °C for 1 h. And then the samples were subjected to SLM treatment to obtain pre-HA/MoS_2-Ti6. The sulfur powder was then sublimed via CVD to get HA/MoS_2-Ti6. Scanning electron microscopy (SEM) was used to observe the surface morphology of Ti6 and HA-Ti6, MoS_2-Ti6, and HA/MoS_2-Ti6. The HA, MoS_2, and HA/MoS_2 were uniformly distributed on Ti6 surface (Figures S1 and 1b). Besides, the thickness of the HA/MoS_2 coating on the Ti6 plate was observed by cross-sectional image, and the thickness of HA/MoS_2 coating was about 4.95 μm, and the coating was well clad with the substrate (Figure 1c). Figure 1d shows X-ray diffraction (XRD) spectra of Ti6, HA-Ti6, MoS_2-Ti6, and HA/MoS_2-Ti6. Except for the obvious Ti6 peak, in MoS_2-Ti6, and HA/MoS_2-Ti6, one distinct peak at 14.3° can be indexed as the (002) peak of MoS_2 [28]. On the other hand, two distinct diffraction peaks at 31.9° and 33.0° in HA-Ti6 and HA/MoS_2-Ti6 can be indexed as the (211) and (300) crystal faces of HA [29]. It proved that the HA/MoS_2 composite was successfully clad on the Ti6 plate. Figure 1e shows the transmission electron microscopy (TEM) image of the HA/MoS_2 separated from HA/MoS_2-Ti6. The lattice spacing of 0.60 and 0.28 nm corresponded to (002) plane of MoS_2 and (002) plane of HA, respectively [30,31]. Furthermore, the TEM and corresponding element mapping images of HA/MoS_2 showed that Ca, P, Mo, and S elements were uniformly distributed in HA/MoS_2 (Figure 1f,g), which suggested that HA and MoS_2 were laser cladding together. The X-ray photoelectron spectroscopy (XPS) spectra of the HA-Ti6, MoS_2-Ti6, and HA/MoS_2-Ti6 were shown in Figure 1h. Both HA-Ti6 and HA/MoS_2-Ti6 contained O, Ca, and P elements. Meanwhile, there was a peak of Mo element in HA/MoS_2-Ti6 and MoS_2-Ti6. The high-resolution spectra of Mo 3d and S 2p for HA/MoS_2-Ti6 were further analyzed (Figure 1i,j). As for Mo 3d, there were three peaks with binding energies around 235.6, 232.4, and 229.2 eV, which could be assigned to the peaks of Mo $3d_{3/2,}$ Mo $3d_{3/2}$, and Mo $3d_{5/2}$. As for S 2p, the two peaks at 162.0 and 163.6 eV were identical with S 2p3/2 and S 2p1/2, respectively [32]. The contact angles of Ti6, HA-Ti6, MoS_2-Ti6, and HA/MoS_2-Ti6 were 79.8°, 38.6°, 39.1°, and 36.3°, respectively (Figure 1k). The result suggested that the hydrophilicity of the samples' surface after the treatment of SLM.

3.2. Mechanism of Enhanced Photocatalytic Properties of HA/MoS_2-Ti6 and Antibacterial Effect of HA/MoS_2-Ti6

The electric structure of HA/MoS_2 was assessed by the corresponding differential charge density (DCD) and density of electronic states (DOS) via the first-principles calculations after structure optimization (Figure 2a,b). DCD represented the gain and loss of charge. The warm and cool color means getting electrons and losing electrons, respectively. The DCD image of the HA/MoS_2 heterostructure suggested that the electrons were transferred from MoS_2 to HA (Figure 2a). DOS showed the number of electronic states of HA/MoS_2, implying that the primary density of states was offered by Mo, S, and O elements. Based on DFT calculation, the possible mechanism of enhanced photocatalyst activity of HA/MoS_2 compared with MoS_2 is shown in Figure 2c. When HA/MoS_2 was irradiated by 660 nm light, the electrons and holes from MoS_2 were produced. Then the electrons were transferred to phosphate groups of HA, which limited the electron and hole recombination due to the ability of phosphate to attract electrons and enhanced the photocatalytic activity of HA/MoS_2 [33]. The following experimental results supported our hypothesis. The MoS_2-Ti6 and HA/MoS_2-Ti6 spectra showed an enhanced absorption at 660 nm compared with Ti6 and HA-Ti6. The absorption of HA/MoS_2-Ti6 also showed a minor increase compared with MoS_2-Ti6 at 660 nm [23]. Those suggested that HA/MoS_2-Ti6 harvested more 660 nm light and had the possibility of better photocatalytic ability [34]. Next, the photoluminescence (PL) spectra were used to evaluate the electron-hole pairs' combination efficiency of HA-Ti6, MoS_2-Ti6, and HA/MoS_2-Ti6. HA/MoS_2-Ti6 was lowest compared with HA-Ti6 and MoS_2-Ti6, which indicated that the charge combination

efficiency of HA/MoS_2-Ti6 was lower than that of MoS_2-Ti6 and HA-Ti6 (Figure 2d) [22]. Then, as shown in Figure 2e, the photocurrent of HA/MoS_2-Ti6 was higher than Ti6, HA-Ti6, and MoS_2-Ti6, indicating that HA/MoS_2-Ti6 had the highest yields of photo-induced electrons under 660 nm light irradiation [22]. Meanwhile, the photocurrent was produced steadily and periodically, suggesting that HA/MoS_2-Ti6 could repeatedly produce photo-induced electrons under 660 nm light irradiation. Those results further demonstrated that the photocatalytic activity of HA/MoS_2-Ti6 was higher than that of individual HA-Ti6 and MoS_2-Ti6.

Under 660 nm light irradiation, different samples' photothermal and photodynamic activity were then evaluated. 2′-7′ dichlorofluorescein diacetate (DCFH-DA) fluorescence probe is generally used to detect ROS [35]. As shown in Figure 2f, ROS yield produced by HA/MoS_2-Ti6 group (23.28 fold compared with t_0) was higher than the ROS yield produced by MoS_2-Ti6 group (10.69 fold), HA-Ti6 group (4.09 fold), and Ti6 group (1.84 fold) after 660 nm light irradiation for 15 min. 1,3-diphenylisobenzofuran (DPBF), terephthalic acid (TA) and nitro blue tetrazolium (NBT) probes were used to identify the $^1O_2$, •OH, and $\bullet O_2^-$, respectively [35,36].

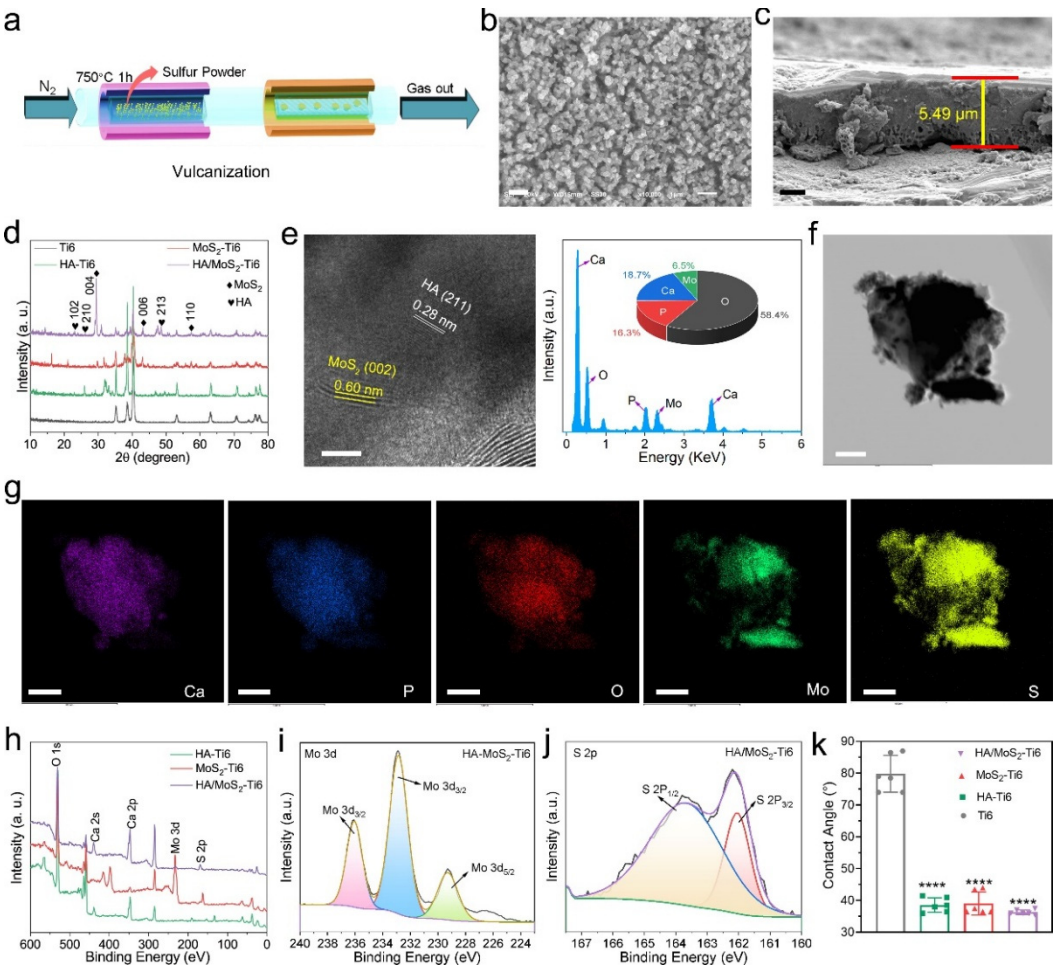

Figure 1. Characterization of HA/MoS_2-Ti6. (**a**) Illustration of vulcanization in the forming process of HA/MoS_2-Ti6. (**b**) SEM image of HA/MoS_2-Ti6. Scale bar: 1 μm. (**c**) Cross-section image of HA/MoS_2-Ti6. Scale bar: 2 μm. (**d**) XRD patterns of different samples (Ti6, HA-Ti6, MoS_2-Ti6, and HA/MoS_2-Ti6). (**e**) TEM and HRTEM images of HA/MoS_2 nanocomposite, which was scraped from HA/MoS_2-Ti6. The left scale bar is 200 nm, and the right scale bar is 5 nm. (**f**,**g**) HRTEM image and element mapping images of HA/MoS_2-Ti6. Scale bar: 200 nm. (**h**) XPS spectra of different samples (HA-Ti6, MoS_2-Ti6, and HA/MoS_2-Ti6). (**i**) High-resolution XPS spectra of Mo of HA/MoS_2-Ti6 sample. (**j**) High-resolution XPS spectra of S of HA/MoS_2-Ti6 sample. (**k**) Water contact angles of Ti6, HA-Ti6, MoS_2-Ti6, and HA/MoS_2-Ti6. Data represent the mean ± standard deviation (n = 3 biologically independent samples). Significance was assessed using a one-way analysis of variance (ANOVA) with Dunnett's multiple comparisons. **** $p < 0.0001$.

As shown in Figure 2g, the DPBF fluorescence intensity decreased over time, suggesting that the ROS species contained $^1O_2$. The fluorescence intensity of TA and NBT was not changed at different moments (0 min, 10 min, 20 min, and 30 min), suggesting that there was no •OH and $\bullet O_2^-$ production after light irradiation (Figures S2 and S3). The photothermal activity of Ti6, HA-Ti6, MoS_2-Ti6, and HA/MoS_2-Ti6 was further investigated

(Figure S4). The enhanced temperature for HA/MoS_2-Ti6 group was 13.3 ℃, which was slightly higher than the MoS_2-Ti6 group (12.5 °C), the HA-Ti6 group (9.7 ℃), and Ti6 group (9.2 ℃) for 10 min, suggesting that HA/MoS_2-Ti6 had almost not photothermal activity under 660 nm light irradiation. The antibacterial effect of HA/MoS_2-Ti6 towards *S. aureus* and *E. coli* was further studied through the plate spread method (Figures 2h, S5, and S6). It can be found that HA/MoS_2-Ti6 exhibited an excellent antibacterial effect after 15 min of light irradiation. The antibacterial activity of HA/MoS_2-Ti6-On (HA/MoS_2-Ti6 under 660 nm light) against *S. aureus* and *E. coli* was 92.99 ± 0.84% and 94.70 ± 3.60%. At the same time, MoS_2-Ti6-On also had a specific antibacterial ability (*S. aureus*, 55.54 ± 5.58% and *E. coli*, 57 ± 4%). Still, the antibacterial effect was not as good as HA/MoS_2-Ti6 due to inadequate PDT activity. On the contrary, there was no significant difference in antibacterial properties for HA-Ti6-On, Ti6-On, and all groups without light irradiation. Although the photothermal and photodynamic activity of HA/MoS_2-Ti6 was poor, the antibacterial ability of HA/MoS_2-Ti6 was great. It indicated something else was involved in the antibacterial activity of HA/MoS_2-Ti6 other than PDT activity. Those will be analyzed in the following part.

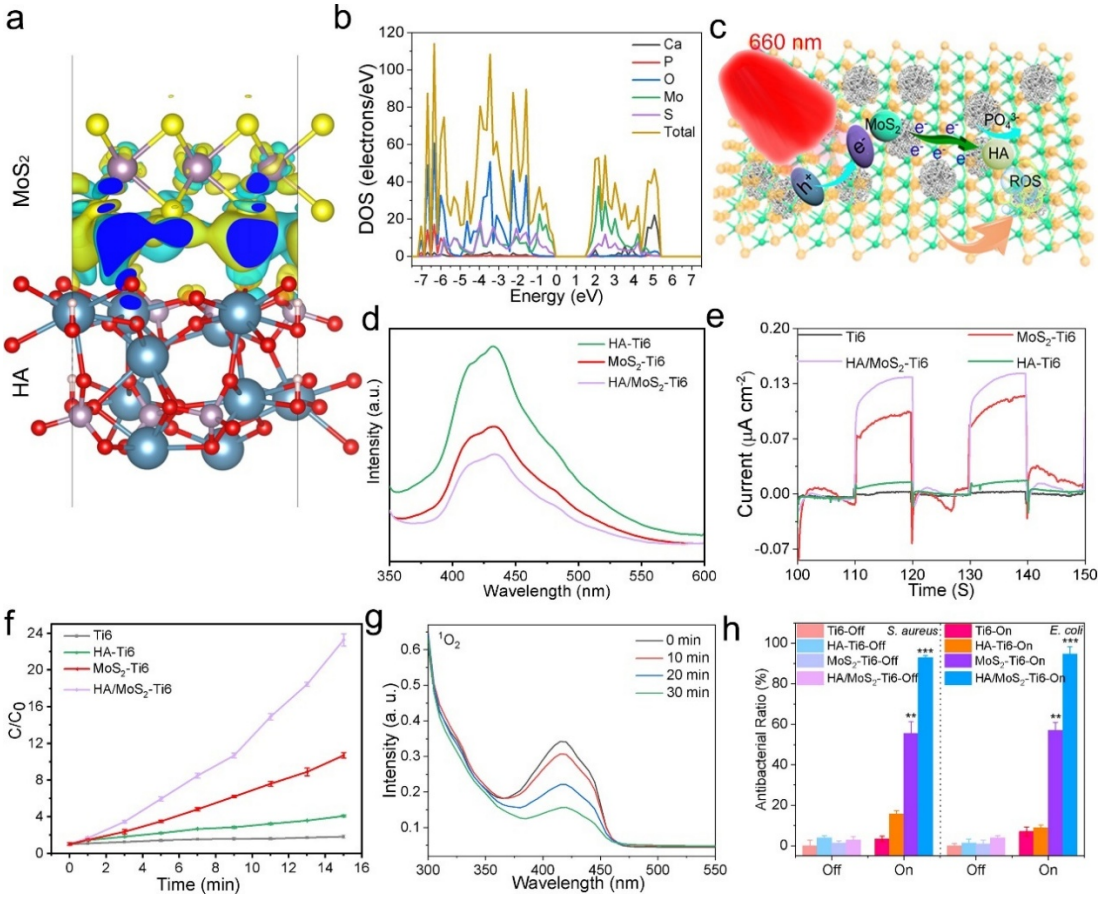

Figure 2. Mechanism of enhanced photocatalytic properties of HA/MoS_2-Ti6 and antibacterial effect of HA/MoS_2-Ti6. (**a**) DCD for HA/MoS_2. The warm color and cool color mean getting electrons and losing electrons, respectively. (**b**) DOS for HA/MoS_2. (**c**) Schematic illustration of the photocatalytic mechanism of HA/MoS_2-Ti6. (**d**) PL spectra of HA-Ti6, MoS_2-Ti6, and HA/MoS_2-Ti6. (**e**) Photocurrent versus time (I-t) curves of Ti6, HA-Ti6, MoS_2-Ti6, and HA/MoS_2-Ti6 under excitation (λex = 660 nm); The dark/light cycle was 10s. (**f**) ROS production of Ti6, HA-Ti6, MoS_2-Ti6, and HA/MoS_2-Ti6 under 660 nm irradiation for different times. (**g**) Absorption spectra of DPBF solution incubated with HA/MoS_2-Ti6 under 660 nm irradiation for different times. (**h**) *S. aureus* and *E. coli* strain counts were calculated from spread-plate assays after treatment with Ti6, HA-Ti6, MoS_2-Ti6, and HA/MoS_2-Ti6 under 660 nm light irradiation or not. Data represent the mean ± standard deviation, n = 3 independent experiments per group, ** $p < 0.01$, *** $p < 0.001$. Statistical significance is calculated with one-way analysis of variance (ANOVA) with Dunnett's multiple comparisons.

3.3. The Antibacterial Mechanism of HA/MoS_2-Ti6 through Nano-Bio Interface under 660 nm Light Irradiation

To further test if the bacteria were killed after different treatments, a live/dead staining assay was performed in which live bacteria were stained green and dead bacteria were stained red. Most bacteria lived during culturing

with different samples without 660 nm irradiation (Figures 3a and S7). The HA/MoS_2-Ti6 and 660 nm irradiation treatment markedly increased the dead bacteria, suggesting that HA/MoS_2-Ti6 could damage the bacterial membrane under light irradiation. The bacterial morphologies were further used to assess the influence of different treatments on bacterial membranes (Figures 3b and S8). In Ti6 and HA-Ti6 groups, the images showed integrated membranes with smooth surfaces, with or without 660 nm irradiation. Similar complete morphology was also observed in the MoS_2-Ti6 and HA/MoS_2-Ti6 groups without 660 nm irradiation. In contrast, the *S. aureus* and *E. coli* membranes were broken and distorted when irradiated by 660 nm. Partially distorted bacteria were found in the MoS_2-Ti6 group. The result further confirmed that the HA/MoS_2-Ti6 group exhibited excellent antibacterial efficacy due to damaging the membrane.

Bacteria own redox potential due to their inert metabolism [37,38]. We hypothesized that the bacterial membrane could form a nano-bio interface with HA/MoS_2-Ti6 to participate in the antibacterial activity of HA/MoS_2-Ti6 due to the overlapped conduction value of HA/MoS_2-Ti6 and the BRP of bacteria. C-type cytochromes (OMCs), the reactive center of the outer-membrane protein, played a vital role in extracellular electron transfer. The octaheme chain transferred the bio-electrons from the bacterial to the electron acceptor [39]. The OMCs were used to stand for the active molecules of the bacterial electron respiratory chain. DFT calculations were further performed to analyze the formation of a nano-bio interface between bacteria and HA/MoS_2-Ti6. The DCD and DOS were used to analyze the direction of transferred electrons. As shown in Figure 3c, the primary electronic states of OMCs were from the s orbit and the p orbit. The central electronic states of HA/MoS_2-Ti6 were offered from p orbit and d orbit (Figure 3d). The main density of states of OMCs-HA/MoS_2-Ti6 was offered from p orbit and d orbit (Figure 3e). As for DOS, green and purple colors represented electron accumulation and depletion, respectively. The color of OMCs and HA/MoS_2 was purple and green, respectively, suggesting that the OMCs' electrons transferred to HA/MoS_2 (Figure 3f). We assumed that the electrons from the bacterial membrane during bacterial respiration participated in the antibacterial process and enhanced the photocatalytic effect through the nano-bio interface. The possible mechanism was illustrated in Figure 3g. When bacteria adhered to the surface of HA/MoS_2-Ti6, bacterial electrons were transferred to HA/MoS_2-Ti6 based on the result of the DFT calculation. Besides, HA/MoS_2-Ti6 would produce electrons and holes after irradiation by 660 nm light. The electrons from bacteria were transferred to HA/MoS_2-Ti6, further enhancing the separation of electrons and holes. These further boosted the photocatalytic activity of HA/MoS_2-Ti6. To assess the influence of different treatments on the redox potential (E_h) of *S. aureus*, a hand-held ORP probe (vs. Ag/AgCl reference) is generally used to obtain E_h. Compared with the E_h value of bacteria cocultured with Ti6 without light, the E_h value of the HA/MoS_2-Ti6-Off group was obviously decreased (Figure 3h). It is suggested that the electron transfer process between HA/MoS_2-Ti6 and bacteria altered the state of bacterial metabolism. After irradiation by 660 nm light, the E_h value of the HA/MoS_2-Ti6-Off group was closer to 0 mV, indicating that the bacterial activity was further damaged. The electrochemical test was performed to evaluate the electron transfer process between HA/MoS_2-Ti6 and bacteria. As shown in Figure 3i, the current value of live *S. aureus*-HA/MoS_2-Ti6 group was higher than HA/MoS_2-Ti6 and dead *S. aureus*-HA/MoS_2-Ti6 groups, suggesting that the electrons from living *S. aureus* were transferred to HA/MoS_2-Ti6 and further enhanced the number of photogenerated electrons of HA/MoS_2-Ti6. The DCFH probe measures the ROS production of different samples [40]. The amount of ROS production in living *S. aureus*-HA/MoS_2-Ti6 was significantly higher than dead *S. aureus*-HA/MoS_2-Ti6, living *S. aureus*, dead *S. aureus,* and HA/MoS_2-Ti6, which suggested that HA/MoS_2-Ti6 culturing with living bacteria enhanced the content of ROS production under 660 nm light irradiation (Figure 3j). Those results demonstrated that the nano-bio interface was successfully formed between bacteria and HA/MoS_2-Ti6, and the nano-bio interface further enhanced ROS production under 660 nm light irradiation.

Microorganisms have acute and flexible regulatory mechanisms to survive and thrive in different environments [41]. To further study the influence of nano-bio interface on bacterial metabolism under 660 nm light irradiation, the intracellular ROS and bacterial membrane potential were measured to assess the state of bacterial metabolism. Live bacteria will produce little ROS during aerobic respiration, and ROS accumulation can disturb bacterial homeostasis [42,43]. As shown in Figures 3k and S9, the intracellular ROS for HA/MoS_2-Ti6-On groups was obviously enhanced compared with the Ti6 group, suggesting that bacterial homeostasis was disturbed after being incubated with HA/MoS_2-Ti6 under 660 nm irradiation. The voltage-sensitive fluorescent dye bis-(1,3-dibutylbarbituric acid) trimethine oxonol (DiBAC4(3)) is generally used to confirm the influence of different treatments on membrane potential, and DiBAC4(3) showed enhanced fluorescence density when bound to depolarized membranes [44]. As shown in Figures 3l and S10, the fluorescence intensities of *S. aureus* and *E. coli* co-incubated with HA/MoS_2-Ti6-On were enhanced due to membrane depolarization. Those results further demonstrated that bacterial metabolism was damaged after being treated by the HA/MoS_2-Ti6-On group.

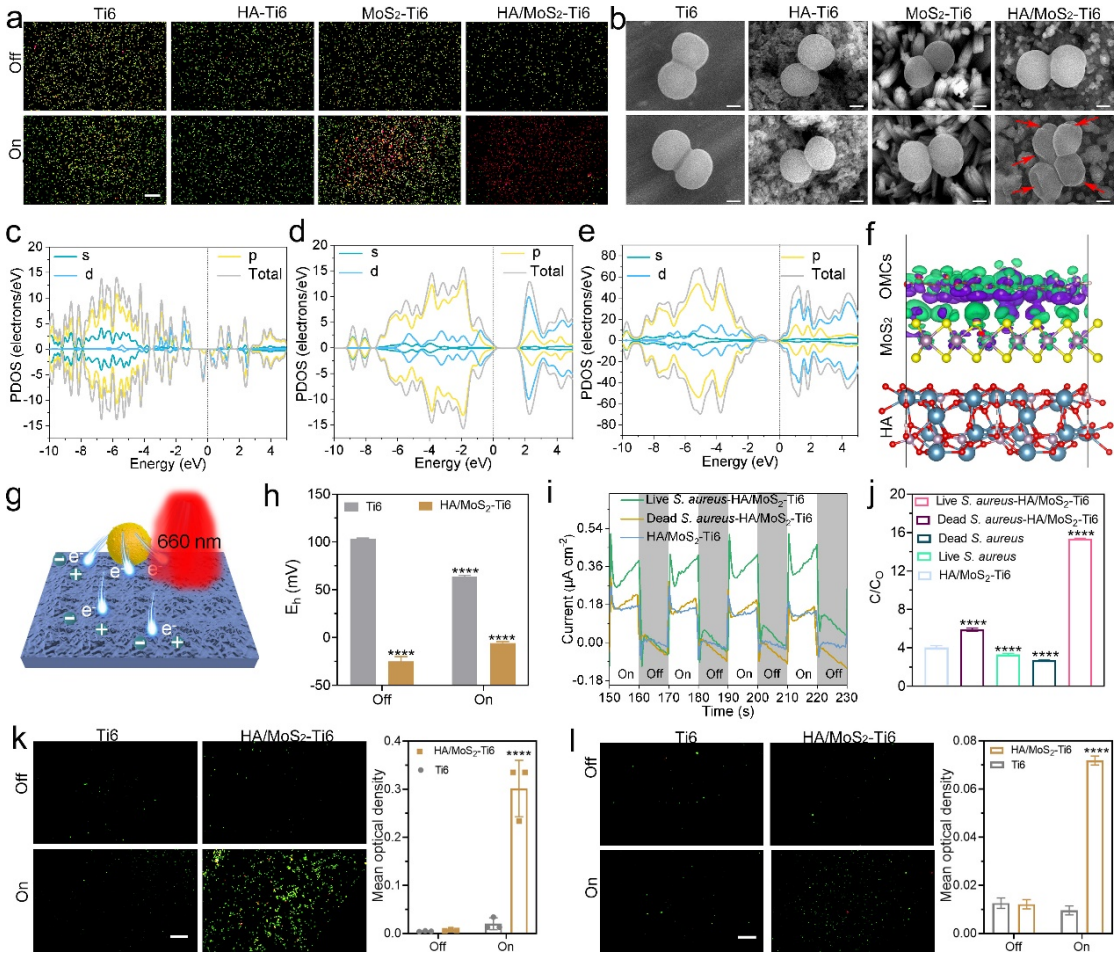

Figure 3. The antibacterial mechanism of HA/MoS_2-Ti6 through nano-bio interface under 660 nm light irradiation. (**a**) The fluorescent images of bacterial dead/living pictures of different samples (Ti6, HA-Ti6, MoS_2-Ti6, and HA/MoS_2-Ti6) with or without 660 nm laser irradiation. The scale bar is 100 μm. (**b**) The bacterial SEM images of different samples (Ti6, HA-Ti6, MoS_2-Ti6, and HA/MoS_2-Ti6) with or without 660 nm laser irradiation. The scale bar is 1 μm. (**c**) PDOS for OMCs. (**d**) PDOS for HA/MoS_2. (**e**) PDOS for OMCs-HA/MoS_2. (**f**) DCD for OMCs-HA/MoS_2. Green and purple isosurfaces represent electron accumulation and depletion, respectively. (**g**) Schematic illustration of the mechanism of enhanced photocatalytic effect through a nano-bio interface. (**h**) Changes in observed redox potential after different treatments. (**i**) Photocurrent versus time (I-t) curves of different samples under excitation (λex = 660 nm); the dark/light cycle was 10 s. (**j**) ROS production of different samples under 660 nm irradiation for different times. (**k**) The fluorescent images of *S. auerus* incubated with different samples (Ti6 and HA/MoS_2-Ti6) under 660 nm laser irradiation. Intracellular ROS was stained with DCFH-DA. The right: the quantitative analysis of DCFH fluorescent density. (**l**) The fluorescent images of *S. auerus* incubated with different samples (Ti6, HA-Ti6, MoS_2-Ti6, and HA/MoS_2-Ti6) under 660 nm laser irradiation. Bacterial membrane potential was stained with DiBAC4(3). The right: the quantitative analysis of membrane potential fluorescent density. n = 3 independent experiments per group, **** $p < 0.0001$. Statistical significance was calculated with one-way ANOVA with Dunnett's multiple comparisons.

3.4. HA/MoS_2-Ti6 Would Not Inhibit the Growth of Cells under Light Irradiation

Besides, the cellular toxicity of different samples (Ti6, HA-Ti6, MoS_2-Ti6, and HA/MoS_2-Ti6) was evaluated by MC3T3-E1 cells and L929 cells. As shown in Figure 4a, the cell morphologies were spread shapes after co-incubation with different samples (Ti6, HA-Ti6, MoS_2-Ti6, and HA/MoS_2-Ti6) at 24 h. The result indicated that Ti6, HA-Ti6, MoS_2-Ti6, and HA/MoS_2-Ti6 had excellent biocompatibility on MC3T3-E1 osteoblasts and L929 fibroblasts. The cell cytotoxic activity of MC3T3-E1 and L929 cells cultured on the surface of different samples was further investigated through 3-(4,5-dimethyl-thiazol-2-yl)-2,5-diphenyltetrazolium bromide (MTT) assay (Figure 4b). The result was the same as that of cell fluorescence staining. Compared with the Ti6 group, the HA/MoS_2-Ti6 group showed better cell viability at 3 days and 7 days, suggesting that HA/MoS_2-Ti6 group had excellent biocompatibility (Figure 4c,d). Laser cladding treatment enhanced the surface hydrophilicity of Ti6, which was conducive to cell adhesion and growth. Meanwhile, the potential difference in the nano-bio interface enhanced mitochondrial activity, further promoting cell growth and proliferation. In addition, the HA/MoS_2

coating triggered Ca^{2+} influx into mitochondria, and the fluctuation of Ca^{2+} promotes cell proliferation [23]. Next, the influence of different groups (Ti6, HA-Ti6, MoS_2-Ti6, and HA/MoS_2-Ti6) on MC3T3-E1 cells migration was further analyzed (Figures S11 and S12). The migration distance in the HA/MoS_2-Ti6 group decreased from 2.63 mm to 1.65 mm after culturing for 12 h, and the space in the HA/MoS_2-Ti6 group was further reduced to 0.45 mm after culturing for 24 h. The result suggested that the HA/MoS_2-Ti6 group promoted osteoblast migration in vitro. Macrophages are the first cells to react to introduced foreign material [45]. So, we chose Raw 264.7 as representative cells to assess the influence of light irradiation. The fluorescent images of Raw 264.7 were obtained (Figure 4e). HA/MoS_2-Ti6-On group showed a spread shape, suggesting that light irradiation did not influence Raw 264.7. MTT result presented a similar tendency (Figure 4f). Next, the Raw 264.7 cell viability was further assessed under irradiation for 5 min. HA/MoS_2-Ti6 showed excellent biocompatibility with/without light irradiation (Figure 4g). The enzyme-linked immunosorbent assay (ELISA) was then used to characterize the state of Raw264.7 (Figure 4h,i), suggesting that the concentration of TNF-α in HA/MoS_2-Ti6-On decreased compared to HA/MoS_2-Ti6-Off, Ti6-On, and Ti6-Off. The concentration of IL-10 in HA/MoS_2-Ti6-On had no difference from HA/MoS_2-Ti6-Off, Ti6-On, and Ti6-Off. Those indicated that the Raw 264.7 was differentiated into M2, which benefited tissue regeneration [35,46,47]. In addition, HA/MoS_2-Ti6 could also induce MC3T3-E1 to differentiate into osteoblasts (Figure S13).

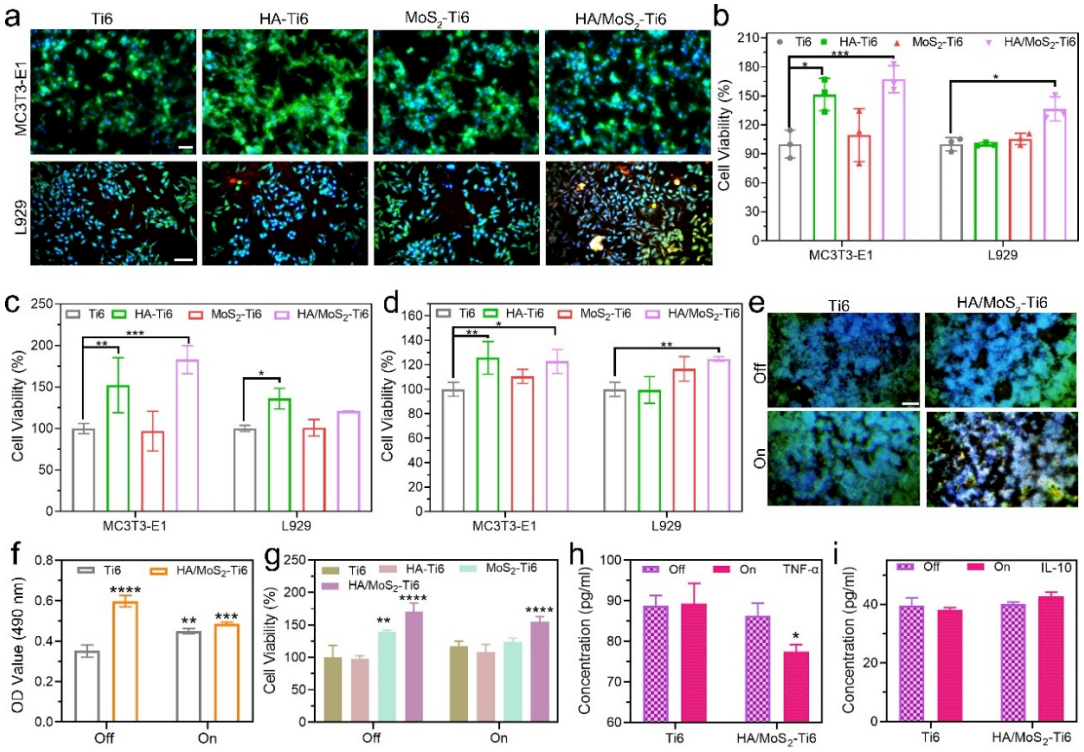

Figure 4. HA/MoS_2-Ti6 would not inhibit the growth of cells under light irradiation. (**a**) Fluorescence images of MC3T3-El cells and L929 cells at 24 h after being incubated with Ti6, HA-Ti6, MoS_2-Ti6, and HA/MoS_2-Ti6. Actin was stained with Fluorescein isothiocyanate (FITC, green) labeled phalloidin, whereas cell nucleus was stained with 4′,6-diamidino-2-phenylindole (DAPI, blue). Scale bar:100 μm. Cell viability of MC3T3-El cells and L929 cells after being incubated with different samples (Ti6, HA-Ti6, MoS_2-Ti6, and HA/MoS_2-Ti6) at (**b**) 1 day, (**c**) 3 days, and (**d**) 7 days. (**e**) Fluorescence images of Raw 264.7 after being incubated with Ti6 and HA/MoS_2-Ti6 under different conditions. Actin was stained with FITC (green) labeled phalloidin, whereas the cell nucleus was stained with DAPI (blue). Scale bar:100 μm. (**f**) Cell viability of Raw 264.7 after being incubated with Ti6 and HA/MoS_2-Ti6 under different conditions. Scale bar:100 μm. (**g**) Cell viability of Raw 264.7 after being incubated with different samples (Ti6, HA-Ti6, MoS_2-Ti6, and HA/MoS_2-Ti6) under 660 nm irradiation for 5 min. (**h**,**i**) Protein levels of TNF-α and IL-10 were quantified by Elisa assay. Data are presented as mean ± standard deviations from a representative experiment. Error bar represents the standard deviation. n = 3 independent experiments per group, * $p < 0.05$, ** $p < 0.01$, *** $p < 0.001$, **** $p < 0.0001$. Statistical significance was calculated with one-way ANOVA with Dunnett's multiple comparisons.

3.5. The Antibacterial Activity of HA/MoS_2-Ti6 In Vivo

Because HA/MoS_2-Ti6 showed great antibacterial activity and excellent biocompatibility, it was investigated for further applications in a Sprague Dawley (SD) rat subcutaneous infection model. The hematoxylin and eosin (H&E) staining and Giemsa staining were used to investigate the therapeutic effects of HA/MoS_2-Ti6 for *S. aureus*-induced subcutaneous infection. As shown in H&E staining (Figure 5a), evident inflammatory cells (marked by light blue arrows) could be seen in the Ti6-Off group. In contrast, there were only a small number of mononuclear inflammatory cells in the HA/MoS_2-Ti6-On group. Similarly, Giemsa staining showed that many remaining bacteria (marked by red arrows) could be observed in the Ti6-Off group. Still, there were very few bacteria in the tissue of the HA/MoS_2-Ti6-On group (Figure 5b). To further quantify the antibacterial effect of the HA/MoS_2-Ti6-On group, the colony-count assay was performed using the tissue fluid around the implant of HA/MoS_2-Ti6 at 2 days (Figure 5c). Compared with the Ti-Off group, the antibacterial rate of HA/MoS_2-Ti6-On group was 99.88%. The result indicated that the HA/MoS_2-Ti6-On group showed a pronounced reduction of *S. aureus* compared with the Ti6-Off group. Those results confirmed the tremendous antibacterial ability of HA/MoS_2-Ti6 against *S. aureus* under 660 nm irradiation.

Then the blood samples of rats were taken after 2 days of treatment. The white blood cell (WBC) counts, neutrophil (Lymph) counts, monocyte (Mon) counts, granulocyte (Gran) counts, and the percentage of neutrophil counts (Lymph%) were tested to assess the inflammatory response (Figure 5d). The Lymph counts, Gran counts, and Lymph% levels of the HA/MoS_2-Ti6-On group were lower than those of the Ti6-Off group due to PDT and electron transfer in the nano-bio interface. Finally, the main organs (lung, liver, spleen, kidney, and heart) were harvested to evaluate the biosafety of HA/MoS_2-Ti6 in vivo (Figure 5e). The HA/MoS_2-Ti6 and Ti6 did not cause damage to the main organ, suggesting that HA/MoS_2-Ti6 and Ti6 showed excellent biosafety.

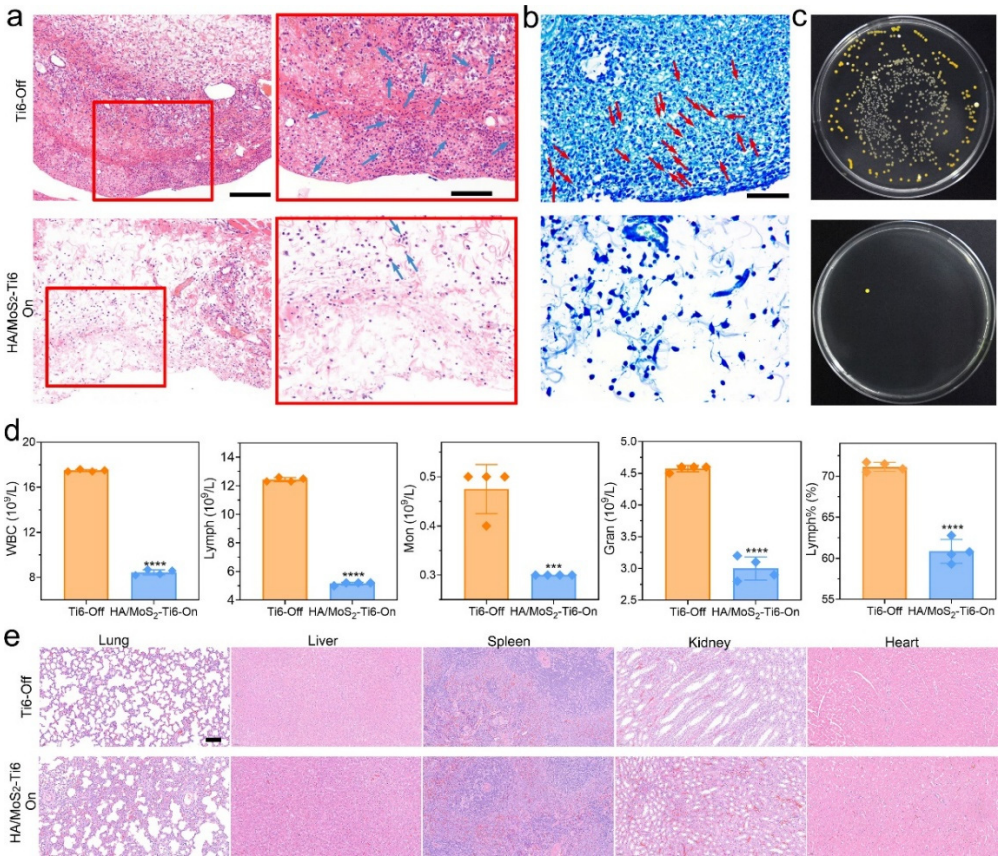

Figure 5. The antibacterial activity of HA/MoS_2-Ti6 in vivo. (**a**) H&E staining images of tissues around the implants. The left scale bar was 200 μm, and the right scale bar was 100 μm. (**b**) The Giemsa staining of tissues around the implants. The left scale bar was 50 μm. (**c**) Remaining bacterial colonies around the tissues of Ti6 and HA/MoS_2-Ti6. (**d**) Parameters of complete blood tests of rats after different treatments. (**e**) H&E staining images of the main organs (lung, liver, spleen, kidney, and heart) from different groups. Scale bar, 100 μm. Data are presented as mean ± standard deviations from a representative experiment. The error bar represents the standard deviation. n = 3 independent experiments per group, *** $p < 0.001$, **** $p < 0.0001$. Statistical significance was calculated with *t* test.

4. Conclusions

In this work, electron transport from bacteria to HA/MoS_2-Ti6 enhanced the PDT effect and killed pathogenic bacteria in vitro and in vivo. The terminal electron flux of bacteria could be transferred to HA/MoS_2-Ti6 based on DFT calculations. Meanwhile, HA/MoS_2-Ti6 would produce photogenerated electrons and holes under 660 nm light irradiation. When bacteria were contacted with HA/MoS_2-Ti6, the content of ROS production was enhanced through the DCFH probe. Using microbial redox power to enhance ROS production for bacterial clearance offered a new means for creating engineered living materials at the biotic/abiotic interface. Physiologically, the damaged bacterial metabolism and ROS produced by HA/MoS_2-Ti6 deforms the membrane integrity and enhances the intracellular ROS level without hindering the growth of MC3T3-E1, L929, and Raw 264.7. Due to its selective antibacterial and excellent biocompatibility, the platform has potential in designing antimicrobial coatings, especially for the surface of medical devices.

Supplementary Materials

The additional data and information can be downloaded at: https://media.sciltp.com/articles/others/250722092 2599930/AAM-1386-SI-FC-done.pdf. Figure S1: The morphology of Ti6, HA-Ti6, MoS_2-Ti6 and HA/MoS_2-Ti6. Figure S2: Absorption spectrum of TA solution. Figure S3: Absorption spectrum of NBT solution. Figure S4: Photothermal heating curves of Ti6, HA-Ti6, MoS2-Ti6, and MoS_2/HA-Ti6 under 660 nm irradiation for different time. Figure S5: Spread plate results of *S. aureus*. Figure S6: Spread plate results of *E. coli*. Figure S7: The fluorescent images of bacterial dead/living pictures of different samples (Ti6, HA-Ti6, MoS_2-Ti6, and HA/MoS_2-Ti6) with or without 660 nm laser irradiation. Figure S8: The bacterial SEM images of different samples (Ti6, HA-Ti6, MoS_2-Ti6, and HA/MoS_2-Ti6) with or without 660 nm laser irradiation. The scale bar is 1 μm. Figure S9: The fluorescent images of *E. coli* incubated with different samples (Ti6 and HA/MoS_2-Ti6) under 660 nm laser irradiation. Figure S10: The fluorescent images of *E. coli* incubated with different samples (Ti6, HA-Ti6, MoS_2-Ti6, and HA/MoS_2-Ti6) under 660 nm laser irradiation. Figure S11: Fluorescence images of MC3T3-El cells at 0 h, 12 h, and 24 h after incubating with Ti6, HA-Ti6, MoS_2-Ti6, and HA/MoS_2-Ti6. Actin was stained red. Figure S12: The quantitative analysis of MC3T3-El migration distance. Figure S13: The osteoblast differentiation ability of MC3T3-E1 osteoblasts after culturing on the surface of different samples.

Author Contributions

J.F.: Conceptualization, Investigation, Methodology, Data analysis, Validation, Writing–original draft; C.W.: Investigation, Methodology, Data analysis; C.M.: Investigation, Methodology, Data analysis; H.J.: Investigation, Methodology, Data analysis; J.S.: Methodology, Data analysis; Z.L.: Methodology, Data analysis; Y.L.: Data analysis; S.Z.: Data analysis; Z.C.: Data analysis; X.L.: Conceptualization, Supervision, Project administration, Writing—review & editing, Funding acquisition. All authors have read and agreed to the published version of the manuscript.

Funding

This work was jointly supported by the National Natural Science Foundation of China (No. 52173251), Yanzhao Young Scientist Project (No. C2023202018), the National Natural Science Foundation of China (No. 52401307), National Natural Science Foundation of China (52471256), and Shenzhen Science and Technology Innovation Committee Project (SGDX20220530111405038).

Institutional Review Board Statement

All animal experiment procedures were approved by the Animal Ethical and Welfare Committee (AEWC) of the Institute of Radiation Medicine, Chinese Academy of Medical Sciences (Approval No. IRM-DWLL-2019087).

Data Availability Statement

The data in the current study are available from the corresponding author on reasonable request.

Conflicts of Interest

The authors declare no conflict of interest.

References

1. Lewis, K.; Lee, R.E.; Brötz-Oesterhelt, R.H.; et al. Sophisticated natural products as antibiotics. *Nature* **2024**, *632*, 39–49.
2. Peng, X.; Gan, Y.; Yang, L.; et al. Biofunctional lipid nanoparticles for precision treatment and prophylaxis of bacterial infections. *Sci. Adv.* **2024**, *10*, eadk9754.
3. Rossiter, S.E.; Fletcher, M.H.; et al. Natural products as platforms to overcome antibiotic resistance. *Chem. Rev.* **2017**, *117*, 12415–12474.
4. Fu, J.; Li, Y.; Zhang, Y.; et al. An engineered pseudo-macrophage for rapid treatment of bacteria-infected osteomyelitis via microwave-excited anti-infection and immunoregulation. *Adv. Mater.* **2021**, *33*, e2102926.
5. Blackmon, S.; Avendano, E.E.; Nirmala, N.; et al. Socioeconomic status and the risk for colonisation or infection with priority bacterial pathogens: A global evidence map. *Lancet Microbe* **2025**, *6*, 100993.
6. Liu, C.; Kong, D.; Hsu, P.; et al. Rapid water disinfection using vertically aligned MoS2 nanofilms and visible light. *Nat. Nanotechnol.* **2016**, *11*, 1098–1104.
7. Gao, Y.; Wang, J.; Hu, D.; et al. Bacteria-targeted supramolecular photosensitizer delivery vehicles for photodynamic ablation against biofilms. *Macromol. Rapid Commun.* **2019**, *40*, e1800763.
8. Ray, P.C.; Khan, S.A.; Singh, A.K.; et al. Nanomaterials for targeted detection and photothermal killing of bacteria. *Chem. Soc. Rev.* **2012**, *41*, 3193–3209.
9. Green, J.; Paget, M.S. Bacterial redox sensors. *Nat. Rev. Microbiol.* **2004**, *2*, 954–966.
10. Liu, D.F.; Li, W.W. Potential-dependent extracellular electron transfer pathways of exoelectrogens. *Curr. Opin. Chem. Biol.* **2020**, *59*, 140–146.
11. Sporer, A.J.; Kahl, L.J.; et al. Redox-based regulation of bacterial development and behavior. *Annu. Rev. Biochem.* **2017**, *86*, 777–797.
12. Nel, A.E.; Mädler, L.; Velegol, D.; et al. Understanding biophysicochemical interactions at the nano–bio interface. *Nat. Mater.* **2009**, *8*, 543–557.
13. Baldus Ilona, B.; Gräter, F. Mechanical Force Can Fine-Tune Redox Potentials of Disulfide Bonds. *Biophys. J.* **2012**, *102*, 622–629.
14. Li, J.; Jiang, M.; Zhou, H.; et al. Vanadium dioxide nanocoating induces tumor cell death through mitochondrial electron transport chain interruption. *Glob. Chall.* **2019**, *3*, 1800058.
15. Sakimoto, K.K.; Wong, A.B.; Yang, P. Self-photosensitization of nonphotosynthetic bacteria for solar-to-chemical production. *Science* **2016**, *351*, 74–76.
16. King, P.; Brown, K.; Harris, D. Light-driven dinitrogen reduction catalyzed by a CdS:nitrogenase MoFe protein biohybrid. *Science* **2016**, *352*, 448–450.
17. Guo, J.; Suástegui, M.; Sakimoto, K.K.; et al. Light-driven fine chemical production in yeast biohybrids. *Science* **2018**, *362*, 813–816.
18. Liu, C.; Colón, B.C.; Ziesack, M.; et al. Water splitting–biosynthetic system with CO_2 reduction efficiencies exceeding photosynthesis. *Science* **2016**, *352*, 1210–1213.
19. Zhang, H.; Liu, H.; Tian, Z.; et al. Bacteria photosensitized by intracellular gold nanoclusters for solar fuel production. *Nat. Nanotechnol.* **2018**, *13*, 900–905.
20. Li, X.; Zhu, H. Two-dimensional MoS2: Properties, preparation, and applications. *J. Materiomics* **2015**, *1*, 33–44.
21. Hendi, A.H.; Osman, A.M.; Khan, I.; et al. Visible light-driven photoelectrocatalytic water splitting using Z-scheme Ag-decorated MoS_2/RGO/$NiWO_4$ heterostructure. *ACS Omega* **2020**, *5*, 31644–31656.
22. Fu, J.; Liu, X.; Liu, X.; et al. Photoelectric-responsive extracellular matrix for bone engineering. *ACS Nano* **2019**, *13*, 13581–13594.
23. Fu, J.; Zhu, W.; Liu, X.; et al. Self-activating anti-infection implant. *Nat. Commun.* **2021**, *12*, 6907.
24. Kresse, G.; Furthmüller, J. Efficiency of ab-initio total energy calculations for metals and semiconductors using a plane-wave basis set. *Comput. Mater. Sci.* **1996**, *6*, 15–50.
25. Blöchl, P.E. Projector augmented-wave method. *Phys. Rev. B* **1994**, *50*, 17953–17979.
26. Perdew, J.P.; Chevary, J.A.; Vosko, S.H.; et al. Atoms, molecules, solids, and surfaces: Applications of the generalized gradient approximation for exchange and correlation. *Phys. Rev. B* **1992**, *46*, 6671–6687.
27. Grimme, S.; Antony, J.; Ehrlich, S.; et al. A consistent and accurate ab initio parametrization of density functional dispersion correction (DFT-D) for the 94 elements H-Pu. *Chem. Phys.* **2010**, *132*, 154104.
28. Li, S.; Liu, Y.; Zhao, X.; et al. Sandwich-like heterostructures of MoS_2/graphene with enlarged interlayer spacing and enhanced hydrophilicity as high-performance cathodes for aqueous zinc-ion batteries. *Adv. Mater.* **2021**, *33*, e2007480.
29. Kottegoda, N.; Sandaruwan, C.; Priyadarshana, G.; et al. Urea-hydroxyapatite nanohybrids for slow release of nitrogen. *ACS Nano* **2017**, *11*, 1214–1221.

30. Bayer, B.C.; Kaindl, R.; Monazam, M.R.A.; et al. Atomic-scale in situ observations of crystallization and restructuring processes in two-dimensional MoS2 films. *ACS Nano* **2018**, *12*, 8758–8769.
31. Yang, C.T.; Li, K.Y.; Meng, F.Q.; et al. ROS-induced HepG2 cell death from hyperthermia using magnetic hydroxyapatite nanoparticles. *Nanotechnology* **2018**, *29*, 375101.
32. Liang, Z.; Xue, Y.; Wang, X.; et al. Co doped MoS2 as cocatalyst considerably improved photocatalytic hydrogen evolution of g-C3N4 in an alkalescent environment. *Chem. Eng. J.* **2021**, *421*, 130016.
33. Umezawa, N.; Shuxin, O.; Ye, J. Theoretical study of high photocatalytic performance of Ag_3PO_4. *Phys. Rev. B* **2011**, *83*, 035202.
34. Li, Y.; Liu, X.; Tan, L.; et al. Rapid sterilization and accelerated wound healing using Zn2+ and graphene oxide modified g-C3N4 under dual light irradiation. *Adv. Funct. Mater.* **2018**, *28*, 1800299.
35. Zhu, Y.; Liu, X.; Wu, J.; et al. Regulation of macrophage polarization through surface topography design to facilitate implant-to-bone osteointegration. *Sci. Adv.* **2021**, *7*, eabf6654.
36. Nosaka, Y.; Nosaka, A.Y. Generation and detection of reactive oxygen species in photocatalysis. *Chem. Rev.* **2017**, *117*, 11302–11336.
37. Bagramyan, K.; Galstyan, A.; Trchounian, A. Redox potential is a determinant in the Escherichia coli anaerobic fermentative growth and survival: Effects of impermeable oxidant. *Bioelectrochemistry* **2000**, *51*, 151–156.
38. Nothling, M.D.; Cao, H.; McKenzie, T.G.; et al. Bacterial redox potential powers controlled radical polymerization. *J. Am. Chem. Soc.* **2021**, *143*, 286–293.
39. Shi, L.; Dong, H.; Reguera, G.; et al. Extracellular electron transfer mechanisms between microorganisms and minerals. *Nat. Rev. Microbiol.* **2016**, *14*, 651–662.
40. Li, Y.; Liu, X.; Tan, L.; et al. Eradicating multidrug-resistant bacteria rapidly using a multi functional g—C_3N_4@Bi_2S_3 nanorod heterojunction with or without antibiotics. *Adv. Funct. Mater.* **2019**, *29*, 1900946.
41. Fang, X.; Kalathil, S.; Divitini, G.; et al. A three-dimensional hybrid electrode with electroactive microbes for efficient electrogenesis and chemical synthesis. *Proc. Nat. Acad. Sci. USA* **2020**, *117*, 5074–5080.
42. Courtney, C.M.; Goodman, S.M.; Nagy, T.A.; et al. Potentiating antibiotics in drug-resistant clinical isolates via stimuli-activated superoxide generation. *Sci. Adv.* **2017**, *3*, e1701776.
43. Lin, W.; Kirschvink, J.L.; Paterson, G.A.; et al. On the origin of microbial magnetoreception. *Natl. Sci. Rev.* **2020**, *7*, 472–479.
44. Martinière, A.; Gibrat, R.; Sentenac, H.; et al. Uncovering pH at both sides of the root plasma membrane interface using noninvasive imaging. *Proc. Nat. Acad. Sci. USA* **2018**, *115*, 6488.
45. Kzhyshkowska, J.; Gudima, A.; Riabov, V.; et al. Macrophage responses to implants: Prospects for personalized medicine. *J. Leukoc. Biol.* **2015**, *98*, 953–962.
46. Fu, J.; Liu, X.; Cui, Z.; et al. Probiotic-based nanoparticles for targeted microbiota modulation and immune restoration in bacterial pneumonia. *Natl. Sci. Rev.* **2023**, *10*, nwac221.
47. Li, Y.; Liu, X.; Cui, Z.; et al. Inflammation and microbiota regulation potentiate pneumonia therapy by biomimetic bacteria and macrophage membrane nanosystem. *Research* **2023**, *6*, 0096.